

Title

Enhanced osteoconductivity on electrically charged titanium implants treated by physicochemical surface modifications methods

Authors

Marc Fernández-Yagüe (1,2), Roman Perez Antoñanzas (1,3), Joan Josep Roa (4), Manus Biggs (2), F. Javier Gil (1,3)*, Marta Pegueroles (1)

Affiliations

(1) Biomaterials, Biomechanics and Tissue Engineering Group, Department of Materials Science and Metallurgical Engineering, Technical University of Catalonia (UPC), EEBE, 08019 Barcelona, Spain

(2) CURAM, Centre for Medical Devices. National University of Ireland, Galway, Galway, Ireland.

(3) Bioengineering Institute of Technology, Universitat Internacional de Catalunya, Barcelona, Spain.

(4) Structural Integrity, Micromechanics and Materials Reliability, Department of Materials Science and Metallurgical Engineering, Technical University of Catalonia (UPC), EEBE, 08019 Barcelona, Spain

* Corresponding Author: Dr F. Javier Gil, School of Dentistry, Universitat Internacional de Catalunya. E-mail: xavier.gil@uic.es telf:(0034) 93 254 18 00 orcid: <https://orcid.org/0000-0003-3265-5071> Address : Campus Sant Cugat, Josep Trueta, s/n 08195 Sant Cugat del Vallès, Barcelona, Spain.

Word count for Abstract: 300

Word count for manuscript: 7613

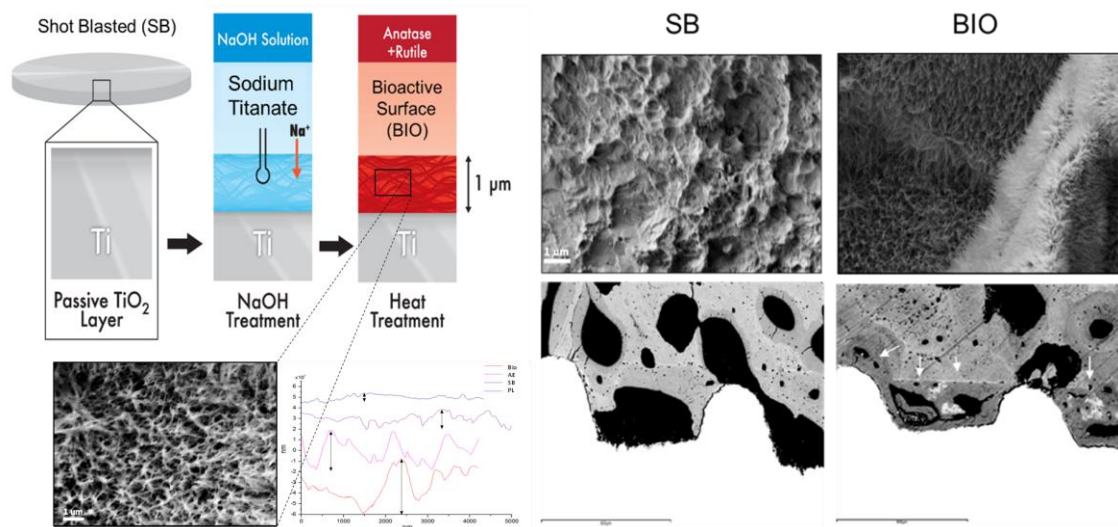
Number of References: 60

Number of figures: 6

Number of tables: 3

Number of Supplementary online-only files, if any: 1

Abstract



Following implantation, dental implant stability can become compromised due to poor bone tissue integration and reactive foreign-body encapsulation. A key tenet of bone tissue engineering is biomimetic design, and in particular, the development of responsive surfaces that promote ion exchange with interfacing tissues, facilitating the ionic events that occur naturally during bone repair, hold promise as orthopedic fixation strategies. Herein, simple thermochemical and oxygen plasma processes are described and assessed *in vivo* as functional approaches for the development of dental implants with enhanced integration potential.

Non-bioactive titanium dental implants treated by shot-blasting and acid-etching (AE) (to produce micro to nanoscale hierarchical topographic structure) induced higher bone implant contact (BIC=53% and 68%) compared to shot-blasted treated (SB) implants (BIC=47% and 49%) at weeks 4 and 8, respectively. Plasma (PL) or thermochemical (BIO) processes were subsequently used to produce a bioactive charged surface by selective ion adsorption as indicated by surface zeta potential changes from -34 mV (SB) to -20mV (PL) or -10 mV (BIO). In addition, an increase on the polar component of surface energy was obtained due to higher number of surface hydroxyl groups as indicated by X-ray photoelectron spectroscopy (XPS) and energy-dispersive X-ray spectroscopy analyses (EDX). *In vivo* results showed that charged implants exhibited enhanced osteoconductivity through ionic surface-tissue exchange (PL, BIC= 69% and 73% and BIO, BIC= 83% and 86 % at weeks 4 and 8 respectively). Furthermore, charged bioactive surfaces (PL and BIO) obtained functional mechanical stability as early as 4 weeks post implantation via increased total bone area (BAT=56% and 59%) ingrowth compared to SB (BAT=35%) and AE (BAT=35%) surfaces. This results correlated positively with clinical evaluation of osseointegration using resonance frequency analysis (RFA). This study describes the development and application of surface functionalization methods to selectively modulate surface charges and enhance implant-bone tissue integration.

Background

Controlled bone-implant integration represents a primary goal of orthopaedic bioengineering. Considering titanium implants for load bearing applications, the required time to achieve a minimum level of osseointegration with mechanical stability is between 8 and 12 weeks^{1,2}. Although titanium surfaces offer improved predictability and superior bone tissue integration relative to alternative metallic implants (i.e. Co-Cr-Mo, stainless steel) titanium is not exempt from risk of failure, especially during the proliferative phase of bone repair (between weeks 4 and 8). Common failure mechanisms range from encapsulation to low primary stability as a result of poor early bony integration. Thus, further research into improving the early integration of implants while controlling the immune-mediated foreign-body response has become of vital importance.

Recently, a number of functionalisation strategies focused on surface modification have been utilized to obtain rapid osseointegration *in vivo*, shorting the time for peri-implant bone healing and remodelling^{1,3}. Indeed, cell-surface interactions can be regarded as the principal defining factor in determining the successful long-term performance and biofunctionality of an orthopaedic device following implantation. The physical surface properties of an implant i.e. topography, surface energy, charge density, and the presence of specific functional groups can directly modulate the tissue response *in vivo*, and influence the onset of fibrosis or controlled osseointegration. Current materials used in bone repair have failed to restore bone function and their lack of biomimicry reflect an increasing need for the development of mechanically biomimetic biomaterials capable of regulating the peri-implant biological activity. Current biomimetic approaches in the design of orthopaedic devices have focused on chemical and/or physical modification of the device surface to more closely mimic the microstructure or topography of bone tissue in order to regulate device integration. Specifically, the incorporation of nanoscale topographical features aims to interact with specific cell-transmembrane receptors (i.e integrins) in attempt to modulate cell adhesion and cytoskeletal tension. These are considered processes that are of vital importance in osteogenesis and osteoconduction

However, encapsulation of metallic implants by fibrous tissue, a physiological process that protects the body from foreign bodies, frequently results in arrested bone repair and subsequent implant failure⁴⁻⁶. To address this challenge, bioactive surfaces have been explored, functional approaches that rely on the formation of a chemically stable bond between the biomaterial surface and the surrounding bone extra cellular matrix without triggering a fibrotic response. This effect was first observed by Hench *et al.* who described the efficacy of calcium phosphate functionalization in promoting implant-bone integration^{7,8}. Different methods for calcium phosphate (CaP) coating of implants to promote bioactivity have been developed and include plasma-spray, CVD or layer by layer self-assembly⁹⁻⁹; however, non-uniformity, delamination and poor bioactivity have been reported limiting their clinical applications¹.

The bone-integration ability of calcium phosphate functionalization derives from its polarized surface that initiates a process of heterogeneous nucleation of supersaturated

physiological fluids. Briefly, ionic exchange between a functional ceramic interface and extracellular calcium and phosphate ions results in the catalyzation of a surface apatite layer. In addition, surface calcium form electrostatic bonds with polyanionic calcium-binding proteins (i.e osteoclastin and osteopontin). Indeed, electrically charged surfaces (polarized) control specific-molecule accumulation including amino acids, ionic groups or proteins (i.e serum albumin) to induce bone repair and repulse undesirable contaminants (i.e hydrocarbons) from the surfaces to prevent host reactions¹²⁻¹⁴.

Recently, it has been showed that the charge of titanium's ceramic layer can be altered by oxidation and chemical modification through different surface modification techniques including alkali-heat and plasma treatments^{15,16}. It is hypothesized that in combination, nano topographical cues together with bone inducing surfaces (polarized) represents an emerging and attractive novel methodology to produce rapid osseointegration of implants. In addition, it still remains unclear whether the efficacy of the bioactive surfaces is due to surface charges density, chemistry or induced nanoscale topography. In this project, we sought to combine appropriated implant chemistry with specific nanoscale topography to accelerate *in vivo* bone-implant integration by rapid repair. We compared the *in vivo* response of two different (apatite-forming) bioactive surfaces with different levels of charge density and two non-bioactive surfaces with different topography levels. We adopted high resolution histomorphometry to precisely quantify the osseointegration level differences between implants at the three relevant time points (2, 4 and 8 weeks) in a minipig animal model. Finally, the results obtained by histomorphometry were compared to those clinically obtained by resonance frequency analysis.

Methods

Materials

Ti c.p grade 3 disks and implants, kindly provided by SOADCO S.L were used for *in vivo* and physicochemical characterization. The surface treatment regimes analyzed in this study were: i) as-machined as control (CTRL), ii) shot blasted with alumina particles (600- μm size) (SB), iii) shot blasted and acid-etched with sulfuric acid (48 % v/v) for 5 minutes at 80°C (AE) , iv) shot blasted, acid-etched and plasma treated with oxygen plasma at low frequency for 20 minutes and immediately immersed in Na^+ rich solution (PL) and v) shot-blasted, alkali and heat-treated (BIO): a bioactive coating was produced by thermo-chemical treatment using 5 M NaOH for 24 hours at 60°C followed by a thermal cycle of 600°C for 1 hour²⁰⁻²². Finally, all implants were sterilized with gamma ray at 25 kGy.

Topographical characterization

The surface roughness of all experimental groups (n=6) was first evaluated qualitatively by field emission scanning electron microscopy (FESEM Supra 40, Carl Zeiss, Germany) with a voltage of 5 KeV. Following Wennerberg and Albrektsson recommendations²¹, surface roughness parameters related to vertical amplitude (S_a , S_q , S_z and S_i), horizontal spacing (S_m) and hybrid vertical and horizontal roughness (S_{dr}) were obtained using White light interferometry (WLI, Wyko NT9300 Optical Profiler Veeco Instruments, USA) in Vertical Scanning Interferometry mode (VSI) and Wyko Vision 232TM software (Veeco, USA). In addition, a Gaussian filter was used to separate waviness and form from roughness (cut-off values, $\lambda_c = 0.8$ mm, for CTRL, SB, AE, PL and BIO surfaces and $\lambda_c = 0.25$ mm. Finally, nanoscale surface topography quantitative analysis was carried out by atomic force microscopy (AFM Multimode, Veeco Instruments, USA) in the tapping mode on an area of 5x5 μm . The vertical amplitude roughness parameters including R_a and R_z were obtained.

Wettability and surface energy

The measurement of the static contact angle (SCA) was carried out by the sessile drop method for non-bioactive surfaces. Conversely, the captive bubble method was used for bioactive samples ($T = 25$ °C) using a water (MilliQ) saturated PMMA chamber. The contact angle measurements (n=6, r=9) were performed using a contact angle video based system (Contact Angle System OCA15plus, Dataphysics, Germany) and analyzed with SCA20 software (Dataphysics, Germany). Following Pegueroles et al.²², the Wenzel equation was applied to account for the effect of surface roughness on surface wettability. Intrinsic contact angle and total surface free energy (SFE) was assessed using two different liquids on each sample: ultra-pure distilled water (MilliQ), and diiodomethane following recommendations by Chesmel et al^{24,25}. Consequently, the SFE components (dispersive and polar) were calculated by means of the Owens and Wendt equation²⁵ as follows:

$$\text{(Total SFE)} \gamma_s = (\text{dispersion component}) \gamma_s^d + (\text{polar component}) \gamma_s^p \quad \left[\frac{\text{mJ}}{\text{m}^2} \right]$$

$$\gamma_{L(1+\cos(CA))} = 2((\gamma_L^d + \gamma_s^d)^{0.5} + (\gamma_L^p + \gamma_s^p)^{0.5}) \quad \left[\frac{\text{mJ}}{\text{m}^2} \right]$$

Chemical characterization

XPS (Perkin-Elmer Physical Electronics, USA) spectra were obtained using a monochromatic X-ray source, Al anode with a $K\alpha$ radiation energy of 1486,6 eV at a take-off angle of 45°. The elements present on the surface were qualitatively evaluated by low-resolution (pass energy=187,85 eV) survey spectra, whereas high-resolution (pass energy=23,5 eV) spectra were taken to establish the binding energy and peak area for quantitative analysis. The positions of the peaks were referenced to C 1s at 285,0 ± 0,2 eV. The determination of the atomic concentration provides the ratio element/sum of all the elements present in the acquired data. The calculation is based on the evaluation of the area of the peak, using the sensitivity factors provided by Perkin-Elmer. All data calculations (peak fitting, integration and background subtraction) were performed with appropriate software (Multipak 6.0, Perkin-Elmer Physical Electronics, USA).

Zeta potential measurements

The measurement of zeta potential for the different surfaces was carried out using an electrokinetic analyzer (SurPASS, Anton Paar) at pH = 7,4. The surface zeta potential was determined after 24 h of surface stabilization in a 0.001M KCl electrolyte solution.

Protein adsorption test

Quartz Crystal Microbalance (QCM-D) with Dissipation Monitoring was used for studying protein adsorption kinetics. Adsorption of Fn on TiO₂-coated sensors from Fn solutions at 50 ug/ml were performed at 37 °C. TiO₂ samples were treated with Argon ion irradiation followed by annealing to generate 4 different type of samples with controllable chemistry (Ti³⁺ or Ti⁴⁺) and roughness (Ra= 1.1nm or 0.3nm).

In vivo study

All animal handling and surgical procedures were conducted according to European Community guidelines for the care and use of laboratory animals (DE 86/609/CEE) and approved by the local veterinary school ethical committee. A total of 96 implants were divided into four groups (SB, AE, PL and BIO) and implanted into 12 female minipigs (5-7 years old). For each time interval, two different surface conditions (in left and right mandible respectively) were assessed per animal. Before euthanasia, the implant stability quotient (ISQ) was measured using resonance frequency analysis (RFA, Osstell ISQ®, Sweden) according to the manufacturer's indications. Animals were euthanized under general anesthesia by an intracardiac injection of barbiturate (Dolethal®, Vetoquinol, France) at 2, 4 and 8 weeks after implantation. The mandibles were radiographed to localize the implant and afterwards they were cut in the buco-lingual direction (Exakt 310, Exakt, Germany) and never overpassing 10 mm width to ensure proper posterior fixation. The samples were fixed in 4 % formaldehyde neutral solution for 7 days, subsequently rinsed in water, dehydrated in graded series of ethanol (from 70 to 100 %) and then embedded into polymethyl methacrylate (Technovit 7200 VLC, Kulzer-Heraeus, Germany). Finally, each implant was sectioned along the longitudinal axis with a diamond circular saw (Leica SP1600, Wetzlar, Germany) and polished. The samples were then observed by SEM using the backscattered electrons (BSE) mode to differentiate between Ti implant, old and new mineralized bone based on their density levels. Global histomorphometry was carried out using a custom-made program based

in an image processing system (Quantimet 500MC, Leica, Cambridge, UK). The percentage of direct contact between mineralized bone and implant was calculated (BIC), bone ingrowth into the threads (BAT) and the bone density 1mm outside the implant threads (ROI) (see figure S2). The other part of the block was processed for histology (Leica SP1600, Germany). The sections were then ground to a final thickness of about 100 μm . Qualitative examinations were performed by light microscopy on stained sections (golden-masson trichrome and Hematoxylin&Eosin)

Statistical analysis

The statistical analysis was performed with ANOVA software using the multiple comparison Fisher's test to determine statistically significant differences between groups ($P < 0.05$). Each data point represents mean \pm standard deviation (SD) of at least three independent experiments.

Results

Surface physicochemical analysis.

The surface microstructure and chemistry analysis by SEM, AFM and XPS are shown in Figures 1, 2 and Table 1. While control surfaces presented a chemically homogenous flat surface ($S_a = 0.02 \mu\text{m}$), SB surfaces were characterized by valleys and peaks of different sizes ($S_a = 3.48 \mu\text{m}$). Similarly, acid-etched samples showed S_a values of $3.61 \mu\text{m}$ and $3.72 \mu\text{m}$ (AE and PL respectively) and presented a more complex nanostructured surface. AFM findings showed a superimposed nanoscale structure (figure 1B) as noted by the increase in R_a values, from 35 nm (SB) to 109 and 112 nm (AE and PL respectively). Interestingly, SB and BIO surfaces presented a similar roughness profile (S_a of $3.48 \mu\text{m}$ and $3.52 \mu\text{m}$ respectively), indicating that alkali-heat treatment did not affect the underlying topography. However, SEM (figure 2) showed that BIO treated materials possessed a rough nano-porous structure ($S_a = 226 \text{ nm}$). Furthermore, chemical analyses revealed increased content of carbon, sodium and calcium, significantly decreasing the signal of Ti present on the surface and increasing the electrical charge of the implant (from -34 mV to -10 mV) (table 3). Finally, the hybrid parameters (S_{dr} and S_m) were similar for all surfaces ($S_m = 101\text{-}145$ and $S_{dr} = 103\text{-}134 \%$) with respect to control samples ($S_m = 22\%$ and $S_{dr} = 35\%$) and only differed significantly for the Bio surfaces ($S_m = 205\%$ and $S_{dr} = 225\%$). While conserving same vertical amplitude values (S_a), nanoscale features spatial density changes ($S_{dr} > 200\%$) in BIO surfaces resulted in distinct surface morphology (figure 2).

Figure 3 shows the SFE components values calculated according to Owens and Wendt²⁵ using the intrinsic contact angles (figure S1). In particular, SFE polar component values for SB and AE were higher (27 and 29 mJ/m^2 respectively) compared to control (13 mJ/m^2) although they increased significantly further for PL and BIO (34 and 37 mJ/m^2 respectively). According to the high resolution XPS of Carbon and Oxygen elements, it was observed that PL and BIO contained larger amount of hydroxyl groups on the surface (higher ratio of OH/TiO_2), which can be explained as result of the thermal oxidation to the Ti-O bonds of the oxidated layer. Conversely on PL, Ti-Ti bonds are easily broken by oxygen plasma and they can react with species of high energy created by plasma to produce hydroxyl groups. Finally, the higher content of O_2 on the SB surface can be attributed to the larger presence of alumina particles and water physically adsorbed.

Histomorphometric analyses

Ninety-six implants were placed without complications or adverse reactions. After two weeks of implantation, it was clearly observed that the BIO implant offered enhanced osseointegration as evidenced by a higher adhesion and bone ingrowth (BIC=49% and BAT=27% respectively) compared to SB (BIC=39 and BAT=23%). In contrast, AE surface presented the lowest BIC and BAT values (19% and 18% respectively) and were associated with increased bone resorption (figure 4). The SB group did not show any change in potential for bone resorption or regeneration relative to control surfaces. Despite the initial low BAT values, AE and PL surfaces promoted bone repair by week 8 as evidenced by increased bone erosion in harversian remodelling sites thus, higher presence of active osteoclastic fronts or cutting cones (figure S4). Of particular interest,

plasma treatment promoted bone growth along the surface indicating a high osteoconductive capability (figure S4). After four weeks, it was observed that BIO surface possessed sufficient mechanical stability to support physiological loading (ISQ= 82%, figure 4), which was mainly related to the high levels of osseointegration achieved (83 % of BIC and 61% of BAT). Similarly, PL surface also reached good mechanical stability by 4 weeks (BIC=70%, Bat=59% and ISQ=80%, figure 4). Finally, after 8 weeks of implantation, all the surfaces achieved a similar degree of bone ingrowth (BAT = 60%) and presented adequate adhesion (BIC=65-90) with respect to the SB surface (BIC=50%). In addition, the microstructure of the bone in contact with the BIO surface presented larger mineralized and structured bone tissue (figure 4).

Discussion

Bone tissue repair after traumatic injury or bone loss following a pathological disease remains an important challenge in the field of orthopaedic and craniofacial surgery²⁶. Current treatments including autografts and allografts are clinically challenging, expensive and linked to health risks and additional surgical procedures. Despite continuous progress in the understanding of biological and physical characteristics of bone microenvironment, lack of biomimetic approaches on current orthopaedic devices reflect the increasing need for improved solutions²⁷. Novel solutions need to employ biologically responsive approaches that focus on modulating bone tissue structure and function. It is increasingly becoming clear that biological systems respond with extreme sensitivity to their environment and therefore to the physico-mechanical properties of an implant surface including surface free energy, charge and topography²⁸. A key principle of medical device technology is to exploit this ability to develop novel surface modification approaches to stimulate early bone tissue regeneration. In this study, we describe a combined physical and chemical surface modification process to induce rapid bone integration.

First, we developed non-bioactive surfaces following industrially common strategies based on the use of facile processing techniques to regulate bone repair. We fabricated rough surfaces ($S_a > 3.5 \mu\text{m}$) by shot-blasting as described previously in our studies to obtain improved cell adhesion and osteospecific differentiation^{22,29-31}. Subsequently, chemical acid etching (AE) was used to significantly alter the topography and confer a hierarchical micro to nanoscale topography³²⁻³⁵. Treatment with acid generated a superimposed nanotopography (nanopits of 4-6 nm) which represents a 3-fold increase on the overall nanoroughness (table 1 and figure S1 A), elimination of physis adsorbed contaminants and electrolyte residues and thicker (10-15 nm) homogenous oxide layer (TiO_2) on the surface as observed by XPS analysis and SEM structural analysis (figure 3). Although both modifications SB and AE (termed subtraction methods³⁶) did not provide significantly higher total free surface energy (47 mJ/m^2) compared to CTRL (39 mJ/m^2); surface interactions with polar components (as indicated in figure 3) increased from 16 to 28 mJ/m^2 , which plays an important role in protein adsorption, cell attachment and bone growth¹⁸⁻²⁰.

Bone repair requires synergistic coordination between different cellular functions including cell adhesion and differentiation that are highly regulated by the microenvironment³⁷⁻⁴². Substrate adhesion allows cells to attach and sense the physicomachanical properties of the extracellular matrix (ECM) via transmembrane integrin receptors⁴³⁻⁴⁵. In turn, differentiation of bone progenitors cells is regulated by ECM chemical factors⁴⁶⁻⁴⁹, but recent studies suggest that electrical properties (electrical charges) of the ECM might also play an important role on cell signalling and bone repair⁵⁰⁻⁵⁵. Surface electrical charges and streaming potentials resulting from ionic exchanges can produce electrical cues necessary to regulate cell function^{56,57}. In this study, we fabricated an electrically charged bioactive surface via thermochemical treatment or plasma treatment that promotes ion exchange with the surrounding media. However, since these modifications have also a simultaneous impact on the topography and chemistry, it becomes unclear the individual effect of roughness or charge surface. To unravel and assess each parameter effect, we investigated the adsorption of fibronectin (Fn) on mono-crystals of TiO_2 with controllable chemistry and topography (figure S6 and S7) using confocal microscopy, AFM and quartz crystal microbalance (QCM-D) measurements. Overall, the results showed an increase on the amount of Fn

adsorption with decreasing roughness and increasing surface charge, highlighting the importance of surface charge. In our *in vivo* experiment, in order to decouple the nanoscale topography effect from the ionic exchange effect, we fabricated a nanostructured surface with zeta potential changing from -29 mV (AE) to -20 mV using oxygen plasma treatment (PL)^{9,18,59-60}. The change on surface charge is attributed to an increase on OH/TiO₂ ratio (2.7) compared to AE (0.7). Finally, after immersion in Na⁺ rich solution, the surface becomes more positively charged (figure S3). As shown previously by Pegueroles et al⁶², surfaces with increased OH⁻ groups (surface free energy and charge) adsorb larger amounts of Fn and provides a higher number of specific cell-binding sites. Interestingly, cells on Fn-coated Ti surfaces showed a differential expression of $\alpha_5\beta_1$ integrin, showing that cells might change from a relaxed state to a tensioned state.

There is a consensus in the tissue engineering community that directed cell adhesion and biomaterials toxicity are associated with different types of interaction between ECM molecules and biomaterial surface including dispersive and specially polar interactions (SFE components)⁶³. Dispersive interactions are always present since they are caused by temporary fluctuations of the charge distributions (i.e van der Waals interaction); however polar interactions comprises interactions between permanent and induced dipoles (i.e. hydrogen bonds) and can be modulated. Following plasma treatment, surfaces presented higher surface free energy polar component and were substantially more hydrophilic compared to SB and AE surfaces. It is reasoned that plasma bombardment generates hydroxyl groups on the surface via hydrolysis (if partial) of oxide layer (hydrated by atmospheric water vapor) and therefore interact with Na⁺ therefore modifying the surface electrical charge from negative (-29 mV) to slightly negative (-20 mV). AFM analysis revealed an increased superimposed nanoscale roughness on PL (R_a =112 nm) and Bio (R_a=225 nm) surfaces compared to SB (R_a=34 nm). In addition, chemical composition analysis (EDX) on the surfaces showed values of Na⁺ / Cl⁻ ratio greater than 1, thus demonstrating preferentially absorption of Na⁺ ions on the surface via ionic interaction (figure S3). It is expected that upon contact with body fluids an ionic exchange with protons will occur initiating ionic exchange. As shown in our previous studies, the apatite nucleation on the bioactive surfaces is mainly localized at concave parts with an electrostatic-favoured situation. Thus, increased density of surface charges (increased with nanoroughness) and rapid consumption of calcium ions with limited mobility occurs at the bottom of the concave parts. Wang et al. showed that apatite nucleation is favoured in concave parts where, as a consequence of geometric features, ionic mobility is restricted⁶⁴. The surface charge provides bioactive surfaces with an increased amount of hydroxyl groups, essential for the acceleration of apatite nucleation. Furthermore, specific ionic exchange pattern is also observed in natural bone repair where apatite nucleation appears at the nanometric spaces of the OH⁻ charged organic matrix. The charge on the PL and BIO surfaces is highly dependent on the formation of new Ti-OH⁻ groups. In conclusion, surface roughness (micro and nano), charge and ion concentration mobility in the solution nearby the surface influence apatite nucleation as shown in figure 6 and explained by Bohner et al⁶⁵.

In this study, the *in vivo* response of dental implants with micro (SB) and nanoscale structures were characterized (AE). After 2 weeks of healing, the implants with micro scale structure showed higher values of bone adhesion and ingrowth than for nanostructured surfaces. However, this effect was reversed after 4 weeks of implantation where both adhesion and ingrowth were higher for nanostructured surfaces. In a previous study done by L. Salou et al, similar results were observed where nanostructured implants performed initially worse at 2 weeks but after 4 weeks the trend was reversed⁶⁶. During the last decade, the number of studies that has demonstrated the effect of surface properties on tissue repair has increased considerably^{1,34,66}. To our knowledge, most of the studies focus on topographical changes to direct cell response and bone healing; only few studies have compared nanostructured surfaces with different charge density with a successful bioactive surface. Plasma treatment is relatively simple process and has been shown to influence the wettability and surface charge density. Proliferation and differentiation of preosteoblastic cells, thus bone formation is influenced by nanoscale topography but, in a greater extent, when combined with chemical and electrical cues. In this study, the electrical charge of a nanostructured surface (PL) was successfully changed by plasma treatment and after immersion, Na⁺ was adsorbed in the surface. PL implants showed an initial low adhesion (BIC 20 %) at two weeks; however after 4 weeks of implantation they showed a rapid healing and reached secondary mechanical stabilization (BIC 70%). Finally, the extent and rate of regeneration of PL surfaces was compared to a well-known biologically active (BIO) surface able to guide specific cell bone differentiation, tissue repair and remodelling through nonspecific adsorption of protein. The bioactive surface (BIO) was created by a thermochemical process that results in the formation of a Na⁺-rich dense gel (amorphous sodium titanate) as shown in the XPS spectrum. Through the exchange of a large number of Na⁺ with H₃O⁺, fluid can negatively charge groups Ti-OH⁻ and as a consequence there is a combination with Ca²⁺ ions positively charged resulting in an amorphous calcium titanate (figure 6). As these ions accumulate, surface acquires an overall positive charge and is at that point when the connection starts with the phosphate groups until the surface becomes an amorphous calcium phosphate. Besides bioactive character, BIO surface presented a nanoscale topography with nanopits of an average size of 7 nm (figure S1) that can enhance osseointegration through the activation of integrin-mediated signalling pathways and as nucleation points for the apatite formation. Ultimately, BIO implant presented a faster and extensive bone healing compared to all other surfaces; however, Pl also presented an exceptional regenerative potential owing its osteoconductive ability. This was noticeable already after four weeks, reaching a BIC of 70 % and BAT of 59% and no adverse tissue reaction was observed since week 2 (Figure S5). The values of resonance frequency after and before the implantation correlated in good manner with those of osseointegration (figure 5).

Conclusion

This study assessed the effect of nanoscale features and surface charges on the bone adhesion and growth of commercial dental implants. After 2 weeks of healing, SB surfaces showed the highest stable level of adhesion and tissue growth. Results after 4 weeks showed that both plasma treated, PL, and bioactive, BIO, surface promoted tissue regeneration demonstrating their intrinsic osteoconductive ability.

Future perspective

Several studies have proved that nanoscale topographical cues are able to determine MSCs fate into osteoblasts. In this study it was observed that bone remodelling rate was further regulated in nanostructured implants by surface charges promoting ionic activity in combination with nanoscale topography. Therefore, incorporation of bioactive character into any medical device might require to integrate mechanical cues using nanoscale topographies and dynamically activated electrical cues to reduce the time of bone regeneration. Nanostructured surfaces that would be responsive to the dynamically changing environment would be of particular interest for implants manufacturers. Piezoelectric or electrical conductive materials may be used to induce surface charges and control the bone resorption or regeneration.

1. Le Guéhennec, L., Soueidan, A., Layrolle, P. & Amouriq, Y. Surface treatments of titanium dental implants for rapid osseointegration. *Dental Materials* **23**, 844–854 (2007).
2. Nedir, R., Bischof, M., Szmukler-Moncler, S., Bernard, J.-P. & Samson, J. Predicting osseointegration by means of implant primary stability. *Clin. Oral Implants Res.* **15**, 520–8 (2004).
3. Calvo-Guirado, J. L. *et al.* Influence of surface treatment on osseointegration of dental implants: histological, histomorphometric and radiological analysis in vivo. *Clin. Oral Investig.* (2014). doi:10.1007/s00784-014-1241-2
4. Helary, G. & Migonney, V. Bioactive polymer coatings to improve bone repair. in *Bone Repair Biomaterials* 309–323 (2009). doi:10.1533/9781845696610.2.309
5. Konttinen, Y. T. *et al.* The microenvironment around total hip replacement prostheses. in *Clinical Orthopaedics and Related Research* 28–38 (2005). doi:10.1097/01.blo.0000150451.50452.da
6. Xue, A. *et al.* Local Foreign-Body Reaction to Commercial Biodegradable Implants: An In Vivo Animal Study. *Cranio-Maxillofacial Trauma Reconstr.* **07**, 027–034 (2014).
7. Hench, L. L. Bioactive materials: The potential for tissue regeneration. in *Journal of Biomedical Materials Research* **41**, 511–518 (1998).
8. Hench, L. L., Roki, N. & Fenn, M. B. Bioactive glasses: Importance of structure and properties in bone regeneration. *J. Mol. Struct.* **1073**, 24–30 (2014).
9. Shi, Q., Qian, Z., Liu, D. & Liu, H. Surface modification of dental titanium implant by layer-by-layer electrostatic self-assembly. *Frontiers in Physiology* **8**, (2017).
10. Metzler, P. *et al.* Nano-crystalline diamond-coated titanium dental implants - A histomorphometric study in adult domestic pigs. *J. Cranio-Maxillofacial Surg.* **41**, 532–538 (2013).
11. Strąkowska, P., Beutner, R., Gnyba, M., Zielinski, A. & Scharnweber, D. Electrochemically assisted deposition of hydroxyapatite on Ti6Al4V substrates covered by CVD diamond films - Coating characterization and first cell biological results. *Mater. Sci. Eng. C* **59**, 624–635 (2016).
12. Nozaki, K. *et al.* Enhanced osteoconductivity of titanium implant by polarization-induced surface charges. *J. Biomed. Mater. Res. - Part A* **102**, 3077–3086 (2014).
13. Salazar-Alvarez, M., Noor, M. R., Soulimane, T., Magner, E. & Tofail, S. A. M. *Interaction of bone proteins and cells with electrostatic domains on hydroxyapatite films. Electrically Active Materials for Medical Devices* (2016). doi:10.1142/9781783269877_0027
14. Kobayashi, T., Nakamura, S. & Yamashita, K. Enhanced osteobonding by negative surface charges of electrically polarized hydroxyapatite. *J. Biomed. Mater. Res.* **57**, 477–484 (2001).
15. Lv, C., T, A. & C, B. Bone response to plasma-cleaned titanium implants. *Int. J. Oral Maxillofac. Implants* **4**, 199–204 (1988).
16. Canullo, L., Genova, T., Wang, H.-L., Carossa, S. & Mussano, F. Plasma of Argon Increases Cell Attachment and Bacterial Decontamination on Different Implant Surfaces. *Int. J. Oral Maxillofac. Implants* **32**, 1315–1323 (2017).
17. Kokubo, T. Bioactive glass ceramics: properties and applications. *Biomaterials* **12**, 155–163 (1991).

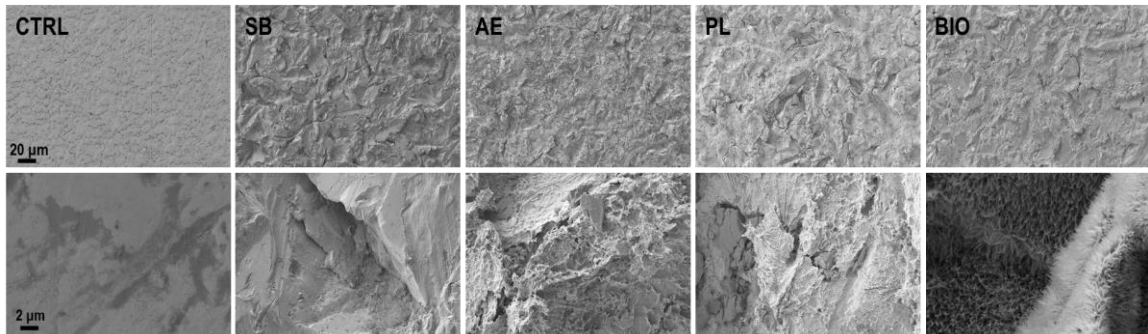
18. Gil, F. J. *et al.* Growth of bioactive surfaces on titanium and its alloys for orthopaedic and dental implants. *Mater. Sci. Eng. C* **22**, 53–60 (2002).
19. Aparicio, C., Gil, F. J., Planell, J. A. & Engel, E. Human-osteoblast proliferation and differentiation on grit-blasted and bioactive titanium for dental applications. in *Journal of Materials Science: Materials in Medicine* **13**, 1105–1111 (2002).
20. Aparicio, C. *et al.* Osseointegration of Grit-Blasted and Bioactive Titanium Implants: Histomorphometry in Minipigs. *Key Eng. Mater.* **254–256**, 737–740 (2004).
21. Wennerberg, A., Albrektsson, T. & Wennerberg A, A. T. Suggested guidelines for the topographic evaluation of implant surfaces. *Int. J. Oral Maxillofac. Implants* **15**, 331–344 (2000).
22. Pegueroles, M. *et al.* Spatial organization of osteoblast fibronectin matrix on titanium surfaces: Effects of roughness, chemical heterogeneity and surface energy. *Acta Biomater.* **6**, 291–301 (2010).
23. Chesmel, K. D., Clark, C. C., Brighton, C. T. & Black, J. Cellular responses to chemical and morphologic aspects of biomaterial surfaces. II. The biosynthetic and migratory response of bone cell populations. *J. Biomed. Mater. Res.* **29**, 1101–1110 (1995).
24. Michiardi, A., Aparicio, C., Ratner, B. D., Planell, J. A. & Gil, J. The influence of surface energy on competitive protein adsorption on oxidized NiTi surfaces. *Biomaterials* **28**, 586–594 (2007).
25. Owens, D. K. & Wendt, R. C. Estimation of the surface free energy of polymers. *J. Appl. Polym. Sci.* **13**, 1741–1747 (1969).
26. Fernandez-yague, M. a *et al.* Biomimetic approaches in bone tissue engineering: Integrating biological and physicochemical strategies. *Adv. Drug Deliv. Rev.* (2014). doi:10.1016/j.addr.2014.09.005
27. Perez, R. A. *et al.* Therapeutically relevant aspects in bone repair and regeneration. *Materials Today* **18**, 573–589 (2015).
28. Wang, Q., Yan, J., Yang, J. & Li, B. Nanomaterials promise better bone repair. *Materials Today* **19**, 451–463 (2016).
29. Aparicio, C. *et al.* Acceleration of apatite nucleation on microrough bioactive titanium for bone-replacing implants. *J. Biomed. Mater. Res. - Part A* **82**, 521–529 (2007).
30. Pegueroles, M., Gil, F. J., Planell, J. A. & Aparicio, C. The influence of blasting and sterilization on static and time-related wettability and surface-energy properties of titanium surfaces. *Surf. Coatings Technol.* **202**, 3470–3479 (2008).
31. Javier Gil, F., Planell, J. A., Padrós, A. & Aparicio, C. The effect of shot blasting and heat treatment on the fatigue behavior of titanium for dental implant applications. *Dent. Mater.* **23**, 486–491 (2007).
32. Ban, S., Iwaya, Y., Kono, H. & Sato, H. Surface modification of titanium by etching in concentrated sulfuric acid. *Dent. Mater.* **22**, 1115–1120 (2006).
33. Takeuchi, M. *et al.* Acid pretreatment of titanium implants. *Biomaterials* **24**, 1821–1827 (2003).
34. Gintaras, J.-D. D. S., Wennerberg-Phd, A., Juodzbalys, G., Saprioniene, M. & Wennerberg, A. New Acid Etched Titanium Dental Implant Surface. *Stomatol. Balt. Dent. Maxillofac. J. Stomatol. Balt. Dent. Maxillofac. J.* **5**, 101–105 (2003).
35. Iwaya, Y. *et al.* Surface properties and biocompatibility of acid-etched titanium. *Dent.*

- Mater. J.* **27**, 415–21 (2008).
36. Jemat, A., Ghazali, M. J., Razali, M. & Otsuka, Y. Surface modifications and their effects on titanium dental implants. *BioMed Research International* **2015**, (2015).
 37. Yin, T. & Li, L. Review series The stem cell niches in bone. *J. Clin. Invest.* **116**, 1195–1201 (2006).
 38. Pirracco, R. P., Marques, A. P. & Reis, R. L. Cell interactions in bone tissue engineering. *Journal of Cellular and Molecular Medicine* **14**, 93–102 (2010).
 39. Petite, H. *et al.* Tissue-engineered bone regeneration. *Nat. Biotechnol.* **18**, 959–963 (2000).
 40. Stevens, M. M. Biomaterials for bone tissue engineering. *Materials Today* **11**, 18–25 (2008).
 41. Shapiro, F. Bone development and its relation to fracture repair. The role of mesenchymal osteoblasts and surface osteoblasts. *European Cells and Materials* **15**, 53–76 (2008).
 42. Sikavitsas, V. I., Temenoff, J. S. & Mikos, A. G. Biomaterials and bone mechanotransduction. *Biomaterials* **22**, 2581–2593 (2001).
 43. Dalby, M. J. *et al.* The control of human mesenchymal cell differentiation using nanoscale symmetry and disorder. *Nat. Mater.* **6**, 407–413 (2007).
 44. Biggs, M. J. P. *et al.* The use of nanoscale topography to modulate the dynamics of adhesion formation in primary osteoblasts and ERK/MAPK signalling in STRO-1+ enriched skeletal stem cells. *Biomaterials* **30**, 5094–5103 (2009).
 45. García, A. J. Get a grip: Integrins in cell-biomaterial interactions. *Biomaterials* **26**, 7525–7529 (2005).
 46. Kingham, E., White, K., Gadegaard, N., Dalby, M. J. & Oreffo, R. O. C. Nanotopographical cues augment mesenchymal differentiation of human embryonic stem cells. *Small* **9**, 2140–2151 (2013).
 47. Urist, M., DeLange, R. & Finerman, G. Bone cell differentiation and growth factors. *Science (80-.)*. **220**, 680–686 (1983).
 48. Chen, G., Deng, C. & Li, Y. P. TGF- β and BMP signaling in osteoblast differentiation and bone formation. *International Journal of Biological Sciences* **8**, 272–288 (2012).
 49. Urist, M. R., DeLange, R. J. & Finerman, G. A. M. Bone cell differentiation and growth factors. *Science (80-.)*. **220**, 680–686 (1983).
 50. Meng, S., Rouabhia, M. & Zhang, Z. Electrical stimulation modulates osteoblast proliferation and bone protein production through heparin-bioactivated conductive scaffolds. *Bioelectromagnetics* **34**, 189–199 (2013).
 51. Aleem, I. S. *et al.* Efficacy of Electrical Stimulators for Bone Healing: A Meta-Analysis of Randomized Sham-Controlled Trials. *Sci. Rep.* **6**, (2016).
 52. Gao, X. & Sevostianov, I. Connection between elastic and electrical properties of cortical bone. *J. Biomech.* **49**, 765–772 (2016).
 53. Singh, S. & Saha, S. Electrical properties of bone: a review. *Clin. Orthop. Relat. Res.* 249–271 (1984).
 54. Kubo, T. Piezoelectricity of bone and electrical callus. *Journal of Orthopaedic Science* **17**, 105–106 (2012).

55. Griffin, M. & Bayat, A. Electrical stimulation in bone healing: critical analysis by evaluating levels of evidence. *Eplasty* **11**, 303–353 (2011).
56. De Aza, P. N., Luklinska, Z. B., Santos, C., Guitian, F. & De Aza, S. Mechanism of bone-like formation on a bioactive implant in vivo. *Biomaterials* **24**, 1437–1445 (2003).
57. Pate, F. D., Hutton, J. T. & Norrish, K. Ionic exchange between soil solution and bone: toward a predictive model. *Appl. Geochemistry* **4**, 303–316 (1989).
58. Yamaguchi, S., Nath, S., Matsushita, T. & Kokubo, T. Controlled release of strontium ions from a bioactive Ti metal with a Ca-enriched surface layer. *Acta Biomater.* **10**, 2282–2289 (2014).
59. Leonard, J. B. K., Bartley, S. M. & Taylor, M. H. Effects of ions and bioactive substances on ovarian contraction in *Fundulus heteroclitus*. *J. Exp. Zool.* **267**, 468–473 (1993).
60. Carvalho, C. N. *et al.* Ions release and pH of calcium hydroxide-, chlorhexidine- and bioactive glass-based endodontic medicaments. *Braz. Dent. J.* **27**, 325–331 (2016).
61. Hoppe, A., Mouriño, V. & Boccaccini, A. R. Therapeutic inorganic ions in bioactive glasses to enhance bone formation and beyond. *Biomater. Sci.* **1**, 254–256 (2013).
62. Pegueroles, M. *et al.* Effect of blasting treatment and Fn coating on MG63 adhesion and differentiation on titanium: A gene expression study using real-time RT-PCR. *J. Mater. Sci. Mater. Med.* (2011). doi:10.1007/s10856-011-4229-3
63. Oshida, Y. Surface Modifications. in *Bioscience and Bioengineering of Titanium Materials* 341–456 (2013). doi:10.1016/B978-0-444-62625-7.00011-X
64. Wang, X. X., Hayakawa, S., Tsuru, K. & Osaka, A. A comparative study of in vitro apatite deposition on heat-, H₂O₂-, and NaOH-treated titanium surfaces. *J. Biomed. Mater. Res.* (2001). doi:10.1002/1097-4636(200102)54:2<172::AID-JBM3>3.0.CO;2-#
65. Bohner, M. & Miron, R. J. A proposed mechanism for material-induced heterotopic ossification. *Materials Today* (2018). doi:10.1016/j.mattod.2018.10.036
66. Salou, L. *et al.* Comparative bone tissue integration of nanostructured and microroughened dental implants. *Nanomedicine* **10**, 741–751 (2015).

Figures

a)



b)

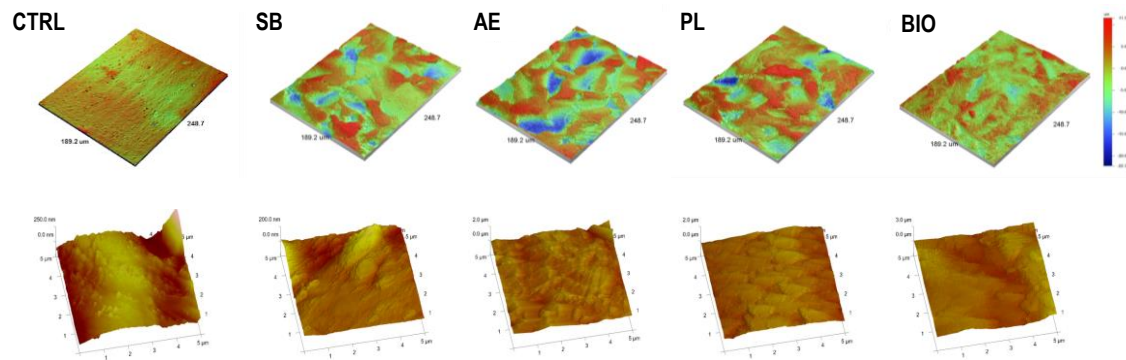


Figure 1. a) SEM images showing the surface morphologies after the different modifications (Ctrl, SB, AE, PL and Bio). b) Representative 3D topography images of the different surfaces using white light interferometry (WLI) and atomic force microscopy (AFM).

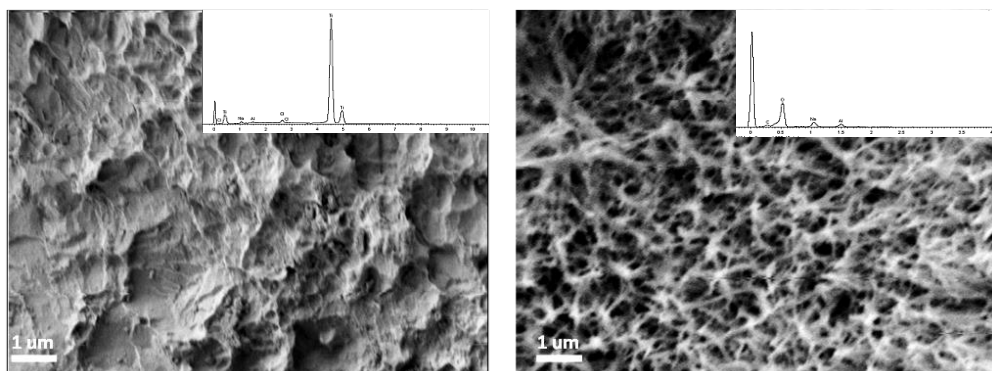


Figure 2. Comparison in chemical composition between the two different nanoscale structures generated by acid etching and thermochemical process using EDS.

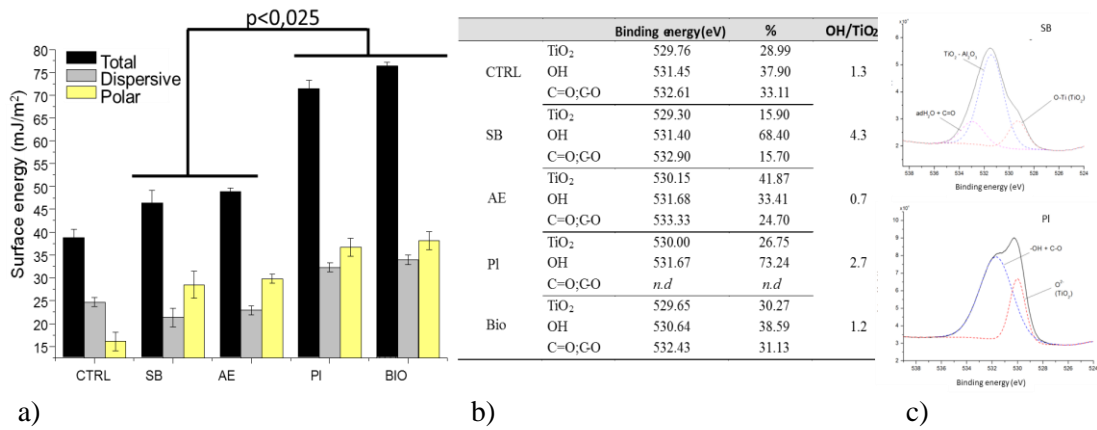


Figure 3. a) Surface free energy (SFE) quantification presenting the total SFE and its components (dispersive and polar) of the different surfaces. b) XPS results showing the increase of OH⁻ groups on the treated surfaces, especially for the plasma treated. c) Deconvoluted signals of XPS showing that despite the SB surfaces presents the highest value of OH⁻, it is accounted mainly for the presence of alumina (Al₂O₃) into the surface or water adsorbed.

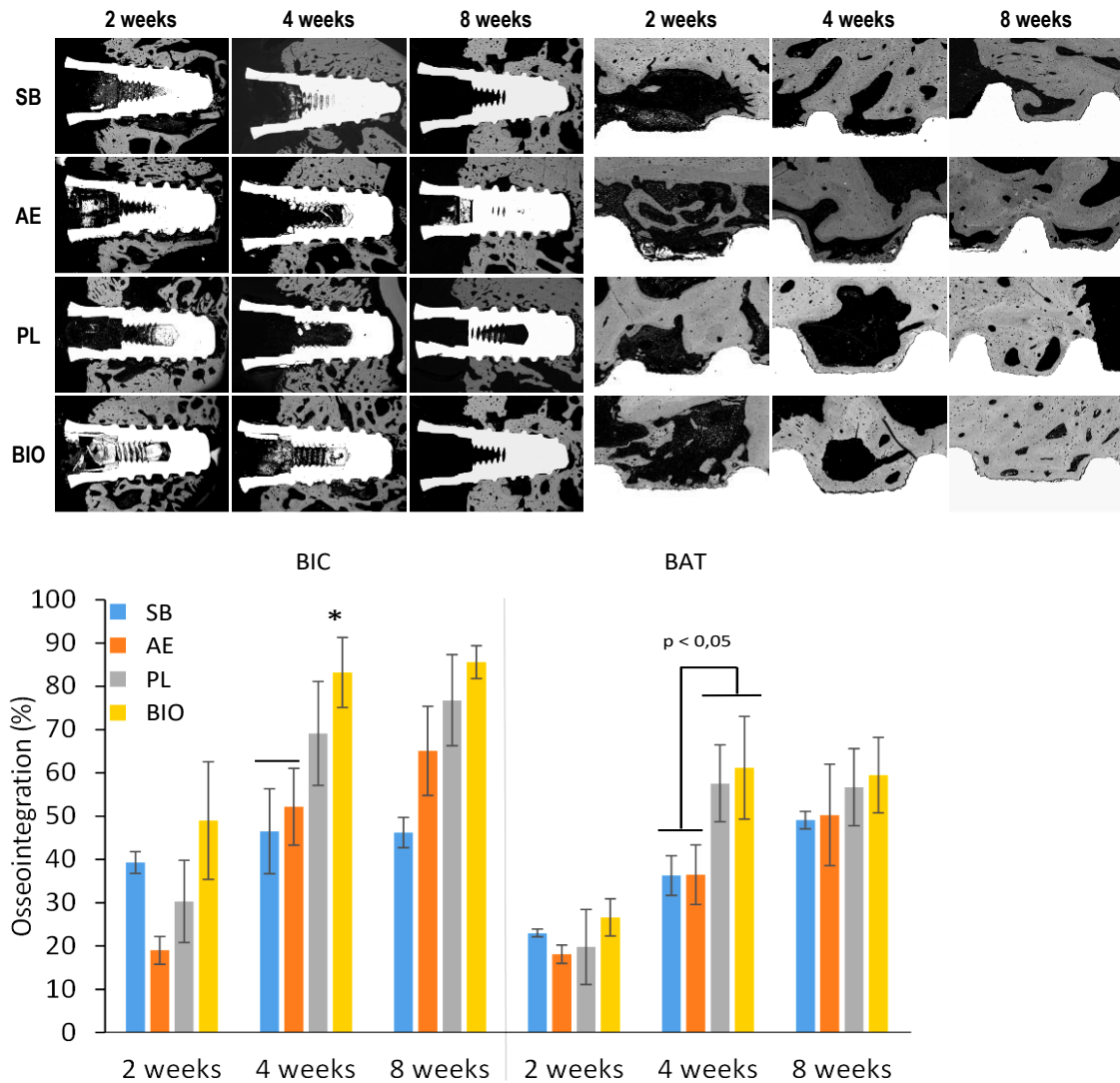


Figure 4. Representative histological SEM images for the 4 different conditions. High magnification SEM images were stitched together with 20% overlapping to form complete image of one implant. At higher magnification, it is possible to appreciate the differential bone ingrowth between different treatments. After 4 weeks of implantation, PI and Bio surface show a higher osteoconductive ability and higher bone repair associated. Graphic representation of osseointegration level characterized by BIC and BAT values for the different surfaces. It is noted a statistically significant difference ($p < 0.05$) at 4 weeks of the groups with BIO and PL respect SB and AE.

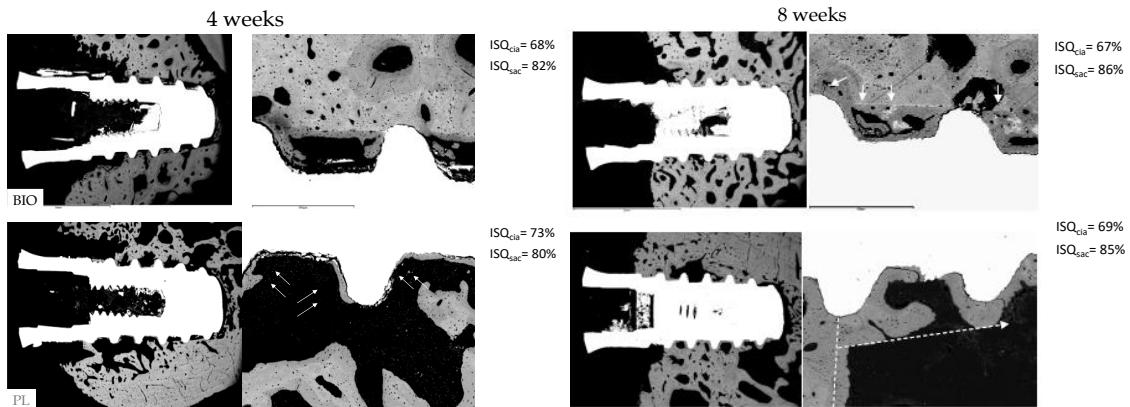


Figure 5. Evidence for secondary (remodeled) tissue and osteoconductive ability on both PI and Bio surfaces after 4 and 8 weeks of implantation. BIO surface shows high level of bone ingrowth at 4 and 8 weeks. It's observed a high amount of new woven bone on the area inside threads separated by the cement line (white arrows) which is going to mature. No bone resorption it's observed. PL surface also presents an excellent osteoconductive ability as evidenced by growth guided by surface at 4 and 8 weeks. At 4 weeks it is observed a slim layer of 3 μm of lamellar bone and at 8 weeks the osteoconductive capability is more evident (white arrows).

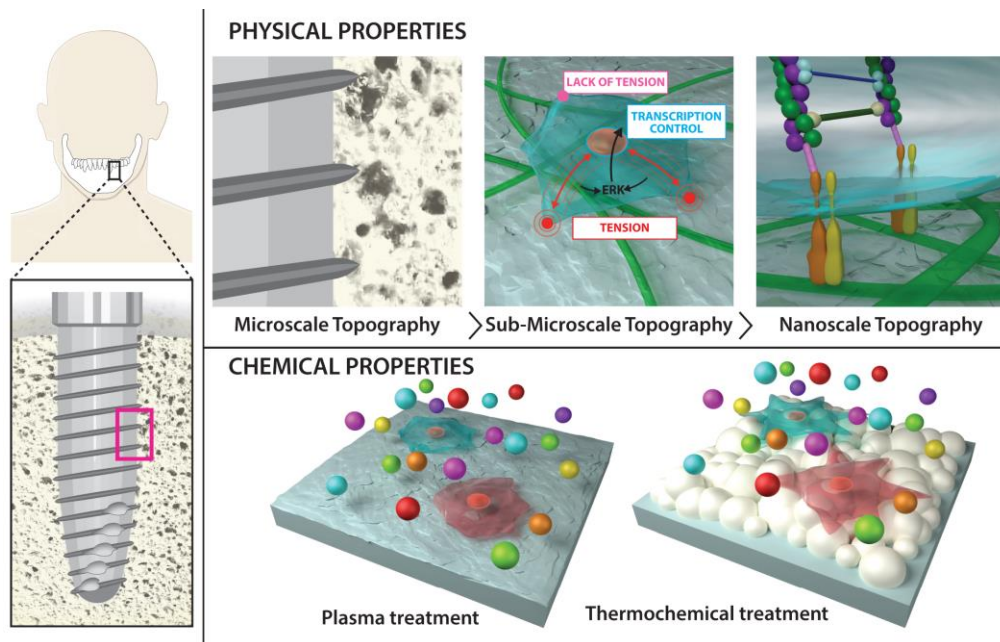


Figure 6. The increase of osteoconductivity of physically and chemically modified surfaces relies on intracellular tension due to nanoscale roughness and rapid consumption of calcium ions for acceleration of apatite formation due to specific ionic body fluid-surface exchange.

Tables

Table 1. Results obtained from interferometry (WLI) and AFM of the topography at two different scales.

Scale	R _a /S _a		R _q /S _q		R _z /S _z		S _m	S _{dr}	S _i
	Nano(nm)	Micro(μm)	Nano(nm)	Micro(μm)	Nano(nm)	Micro(μm)	(μm)	(%)	(-)
CTRL	16.3±1	0.02±0.01	24.8±1	0.02±0.01	190±2	0.02±0.01	22.75±4.51	35.12±4.51	1.00±0.00
SB	34.4±2	3.48±0.41	47.7±2	4.19±0.68	463±2	20.48±2.07	101.58±9.23	103.93±8.51	1.61±0.13
BIO	226±2	3.52±0.54	277±1	4.05±0.56	1617±5	18.59±2.44	205.35±8.23	225.12±12.51	1.75±0.26
PL	112±3	3.61±0.32	140±2	4.59±0.48	1330±4	25.87±2.21	145.15±7.83	113.54±9.51	1.56±0.11
AE	109±2	3.72±0.50	142±3	4.21±0.61	987±3	25.99±2.31	123.21±6.75	134.45±19.46	1.67±0.21

Table 2. Atomic concentrations in percentage of the elements detected by EDS (bulk chemistry) and XPS (surface chemistry). All the elements are expressed in atomic concentration

Scale	C		O		Ti		Cl		Na		N	Ca	Al
	Surface	Bulk	Surface	Bulk	Surface	Bulk	Surface	Bulk	Surface	Bulk	Surface	Bulk	Bulk
CTRL	41.363	44.8	48.957	49.1	6.210	6.10	0.286	n.d	n.d	n.d	3.183	n.d	n.d
SB	59.154	38.1	29.77	51.8	1.345	10.1	n.d	n.d	n.d	n.d.	9.731	n.d	n.d
BIO	43.764	4.54	44.974	60.6	4.139	5.71	0.216	11.1	6.027	9.54	n.d	n.d	1.47
PL	32.498	n.d	51.803	45.9	9.121	44.4	2.111	8.62	3.373	0.59	1.094	0.5	n.d
AE	36.035	n.d	53.126	39.6	9.119	54.2	n.d	6.23	n.d	n.d	1.72	n.d	n.d

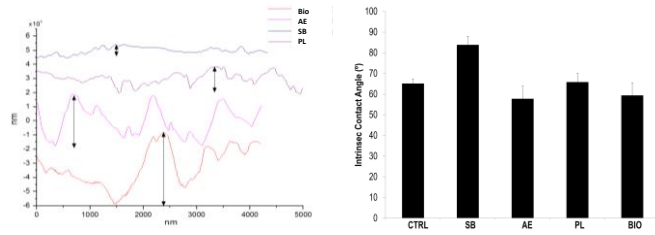
n.d. = non-detected

Table 3. Zeta potential measurements at pH =7.4 for the different surfaces.

	Zeta potential (mV)
CTRL	-25 ± 3
SB	-34 ± 3
BIO	-10 ± 4
PL	-20 ± 5
AE	-29 ± 3

Supplementary information

a)



b)

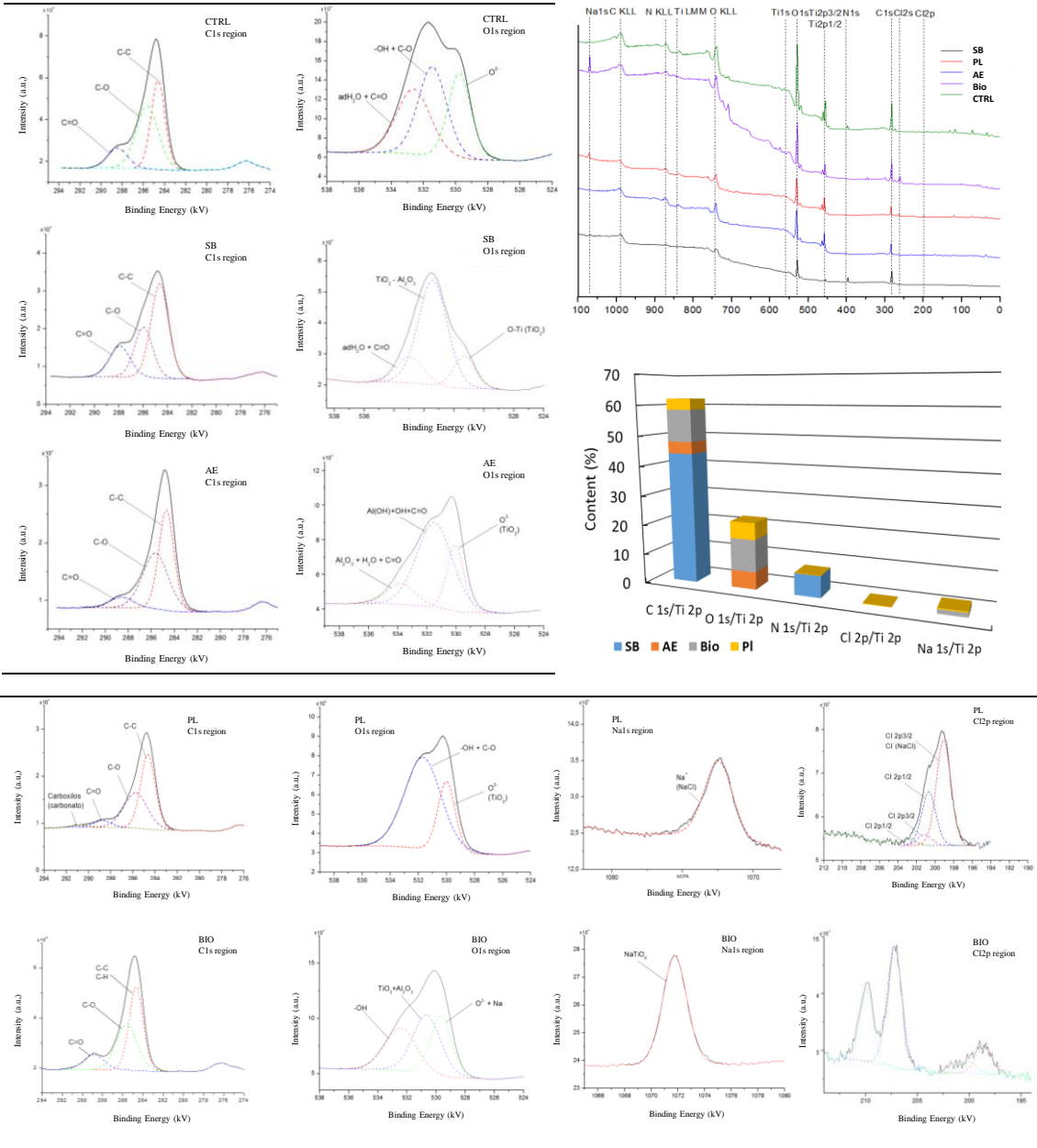


Figure S1. Physicochemical characteristics of the different surfaces using AFM, contact angle and XPS. a) Roughness profiles obtained by AFM b) XPS general spectra (S1) revealed the presence of Oxygen, Carbon and Nitrogen elements and in less amount Na and Cl found on all different titanium surfaces. b) High resolution spectra for all the samples. The higher atomic concentration of O and Ti in PL and BIO samples suggests less hydrocarbons contamination adsorbed onto the surface.

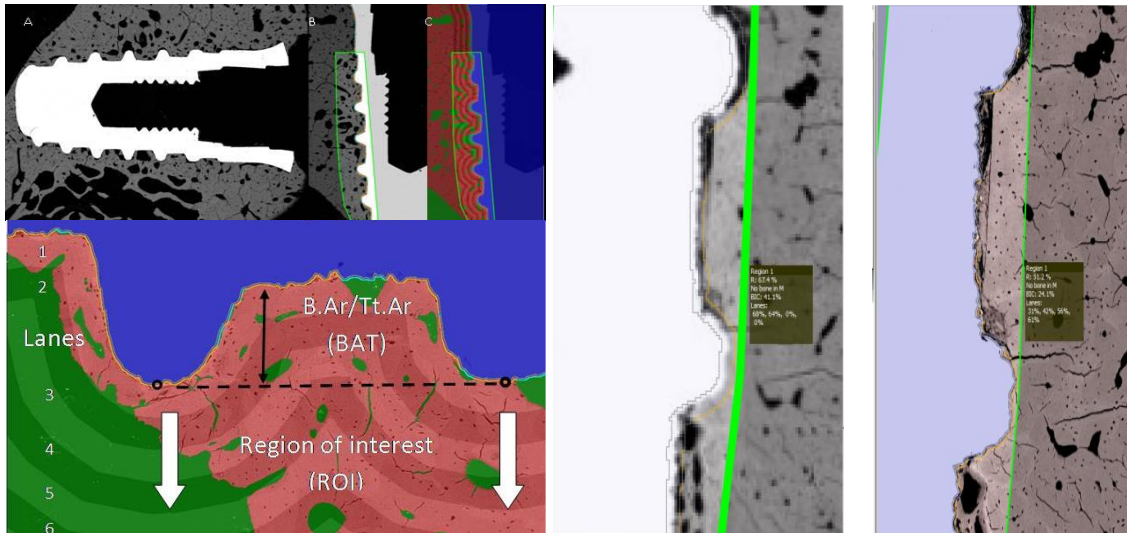


Figure S2. Computer-aided tool image segmentation and quantification of histological parameters. Representative images illustrating the difference in the quantification between low (BIC =41%) and high resolution (BIC=24%) images.

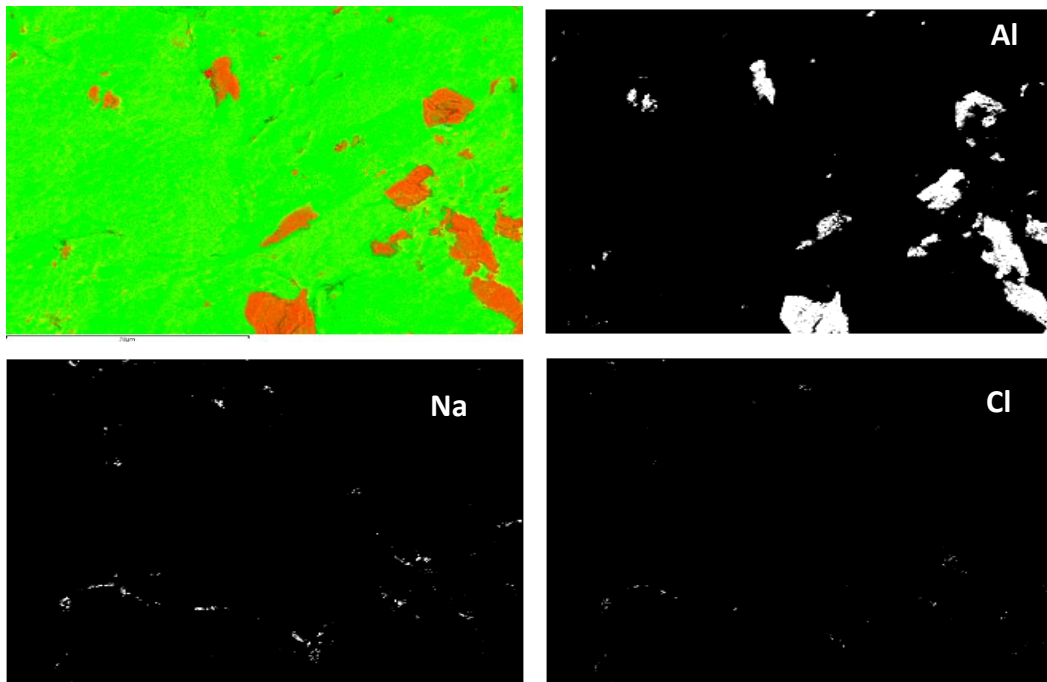


Figure S3. EDS mapping of Al^{2+} , Na^+ and Cl^- on PL samples. In addition, Al_2O_3 particles were found embedded on the surface as result of the shot blasting. This is observed by the presence of Al and the existence of sharp edges on the topography

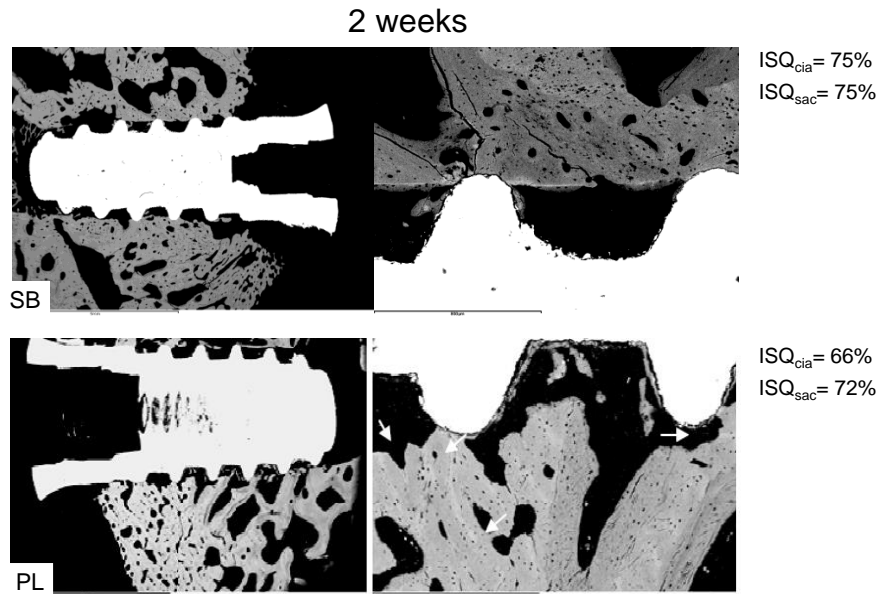


Figure S4. Initiation of proliferative phase after 2 weeks of implantation. It is observed an extensive bone resorption and cutting cones (white arrows) on PL compared to SB.

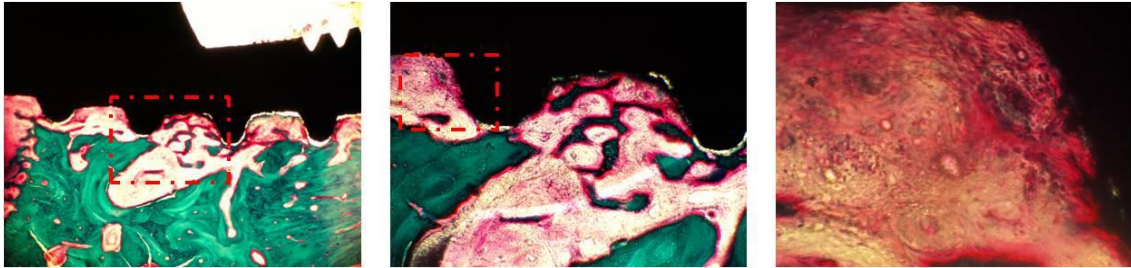


Figure S5. BIO surface at 2 weeks of implantation: Bone is deposited directly upon the metal without any interposition of other tissue components detectable at the level of the light microscope. It is observed a high content of bone matrix onto the surface and a high amount of bone ingrowth.

All the animals tolerated and survived the post-surgical period without any complications. The implants were macroscopically analyzed and neither malpositioning nor signs of inflammation or tissue reaction were found around the implant site. These clinical findings were confirmed radiography and histological analysis that demonstrated no evidence for peri-implant radiolucencies and no increment of inflammatory cells or necrosis signs

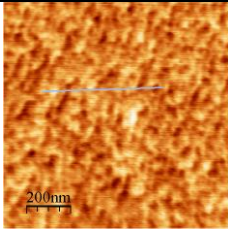
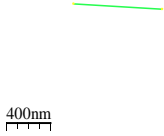
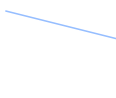
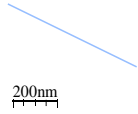
	Ctrl (Ti 4+)	Rough (Ti 4+)	Flat (Ti 3+)	Flat (Ti 4+)
				
Roughness	Ra = 0.16 nm	Ra = 1.1 nm	Ra = 0.4 nm	Ra = 0.3 nm
Zeta Potential	Zeta = -25 mV	Zeta = -34 mV	Zeta = -40 mV	Zeta = -46 mV
Surface Free Energy	SFE = 50,7 mJ/m ²	SFE = 50,4 mJ/m ²	SFE = 45,4 mJ/m ²	SFE = 45,3 mJ/m ²

Figure S6. Physical properties of 4 sample types with different chemistries and roughness.

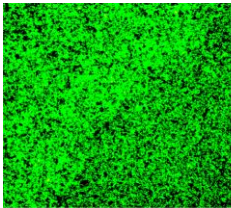
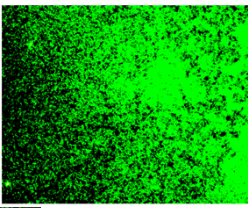
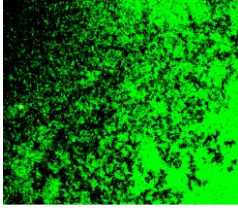
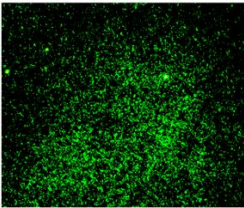
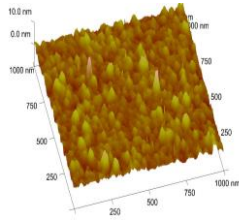
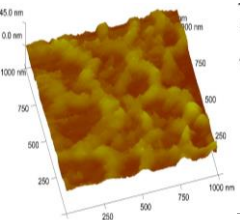
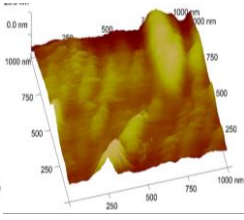
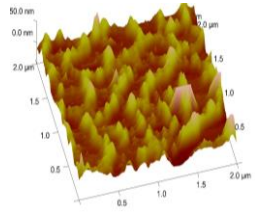
	Ctrl (Ti 4+)	Rough (Ti 4+)	Flat (Ti 3+)	Flat (Ti 4+)
				
Quantity (M-QCD)	16,0 ug/ml	11,2 ug/ml	13,1 ug/ml	6,8 ug/ml
				
Coverage (AFM)	45,9%	42,7 %	35,9 %	35,2%

Figure S7. Physical properties of 4 sample types monocrystals with different chemistries and roughness.

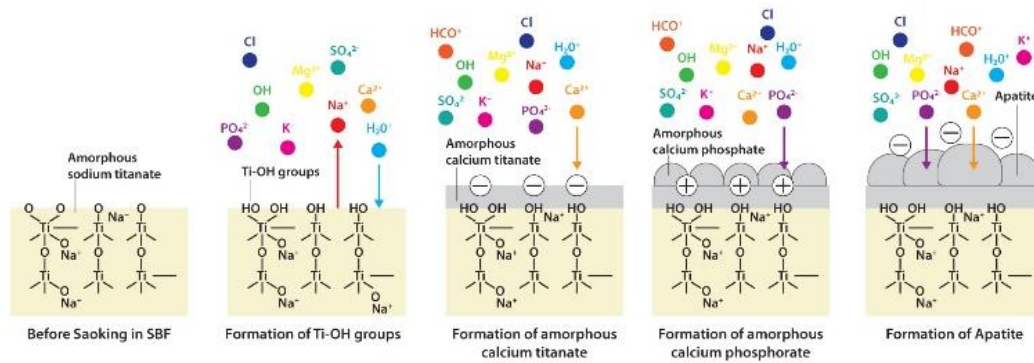


Figure S8. Ionic exchange is initiated by release of positively charged molecules such as Na⁺ (PL and BIO). Subsequently, calcium ions are absorbed on the charged surface and generate an amorphous calcium titanate. Finally, phosphates groups are combined with accumulated calcium ions to initiate crystalline apatite formation. Once formed, apatite continuous to feed on calcium and phosphates ions to grow. Adapted from [1].

	BIC	BAT	ROI
<i>2 weeks</i>			
SB	39.3 ± 2.5	23.0 ± 0.9 a	52.8 ± 2.7a
BIO	49.0 ± 23.6	26.6 ± 4.3 a	57.2 ± 10.8
AE	19.0 ± 3.2	18.1 ± 2.1 b	53.6 ± 19.2 a
PL	30.3 ± 9.5	19.8 ± 8.7 b	54.2 ± 19.7 a
<i>4 weeks</i>			
SB	46.5 ± 9.8	36.3 ± 4.6 a	60.6 ± 16.9
BIO	83.2 ± 8.1	61.2 ± 11.9	58.0 ± 10.5
AE	52.2 ± 12.9	36.5 ± 6.9 a	63.3 ± 8.4 b
PL	69.1 ± 12.0	57.6 ± 28.9	64.6 ± 24.3 b
<i>8 weeks</i>			
SB	46.2 ± 3.5	49.1 ± 2.0	59.6 ± 0.0
BIO	85.6 ± 3.8	59.5 ± 8.7	66.5 ± 11.3
AE	65.1 ± 22.3	50.2 ± 21.7	61.8 ± 18.4
PL	76.8 ± 10.5	56.7 ± 8.9	75.8 ± 8.0

Table S1. Values of the histomorphometric parameters BIC, BAT and ROI for the 4 sample types (SB,AE,PL and BIO) at weeks 2,4 and 8.

	C 1s	O 1s	Ti 2p	N 1s	Mg 1s
Rough (Ti 4+)	50,3	33,4	9,1	2,2	2,2
Flat (Ti 4+)	43	38,7	13,0	1,1	1,3
Flat (Ti 3+)	38,6	38	13,3	2,2	5,9
Ctrl (Ti 4+)	28,0	47,2	20,9	0,4	0,1

Table S2. Physical properties of 4 sample types mono crystals with different chemistries and roughness.

[1] Kim HM, Himeno T, Lee JH, Kokubo T, Nakamura T. Surface potential change in bioactive titanium metal during the process of apatite formation in simulated body fluid. J Biomed Mater Res. 2003; 67A: 1305-1309.